bioRxiv preprint doi: https://doi.org/10.1101/2020.05.16.099390; this version posted May 16, 2020. The copyright holder for this preprint (which was not certified by peer review) is the author/funder. All rights reserved. No reuse allowed without permission.

Multifocal imaging for precise, label-free tracking of fast biological processes in 3D

Jan N. Hansen[1*], An Gong[2], Dagmar Wachten[1,3], René Pascal[2], Alex Turpin[4], Jan F. Jikeli[1†], U. Benjamin Kaupp[2,5†], and Luis Alvarez[2†*]

[1] Institute of Innate Immunity, Medical Faculty, University of Bonn, Bonn, Germany

[2] Center of Advanced European Studies and Research (caesar), Molecular Sensory Systems, Bonn, Germany

[3] Center of Advanced European Studies and Research (caesar), Research Group Molecular Physiology, Bonn, Germany

[4] School of Computing Science, University of Glasgow, Glasgow, UK

[5] Life & Medical Sciences Institute (LIMES), University of Bonn, Bonn, Germany

† J.F.J., U.B.K., and L.A. contributed equally to this work.

* Corresponding authors:

Luis Alvarez, Center of Advanced European Studies and Research, Ludwig-Erhard-Allee 2, 53175 Bonn, Germany, Tel.:+49-228-9656-342, email: luis.alvarez@caesar.de, ORCID: 0000-0002-1027-2291

Jan N. Hansen, Institute of Innate Immunity, Medical Faculty, University of Bonn, Venusberg-Campus 1, 53127 Bonn, Germany, Tel.:+49-228-9656-218, email: jan.hansen@uni-bonn.de, ORCID: 0000-0002-0489-7535

bioRxiv preprint doi: https://doi.org/10.1101/2020.05.16.099390; this version posted May 16, 2020. The copyright holder for this preprint (which was not certified by peer review) is the author/funder. All rights reserved. No reuse allowed without permission.

Abstract

Many biological processes happen on a nano- to millimeter scale and within milliseconds. Established methods such as confocal microscopy are suitable for precise 3D recordings but lack the temporal or spatial resolution to resolve fast 3D processes and require labeled samples. Multifocal imaging (MFI) allows high-speed 3D imaging but suffers from the compromise between spatial resolution and field-of-view (FOV), requiring bright fluorescent labels and limiting its application. Here, we present a new approach for high-resolution, label-free, high-speed MFI, based on dark-field microscopy and operative over large volumes. We introduce a 3D reconstruction algorithm that increases resolution and depth of the sampled volume without compromising speed and FOV. This allowed us to characterize the flagellar beat of human sperm and surrounding fluid flow with a precision below the Abbe limit, in a large volume, and at high speed. Our MFI concept is cost-effective, can be easily built, and does not rely on object labeling, making it broadly applicable.

Introduction

Life happens in three dimensions (3D). Organisms, cells, and sub-cellular compartments continuously undergo 3D movements. A vast number of biological processes take place at the micrometer to millimeter scale within milliseconds. For example, within a second, insects flap their wings 100 to 400 times [1,2], microorganisms swim 0.5 to 50 body lengths [3-5], cilia and flagella beat up to 100 times [6,7], and the cytoplasm of plants streams over a distance of 100 µm [8]. Although methods such as confocal and light-sheet microscopy allow precise 3D recordings, these techniques lack either the time or the spatial resolution to resolve fast biological processes in 3D. Rapid 3D movements can be studied by two complementary high-speed microscopy methods: digital holographic microscopy (DHM) [5,9-12] and multifocal imaging (MFI) [13-16].

bioRxiv preprint doi: https://doi.org/10.1101/2020.05.16.099390; this version posted May 16, 2020. The copyright holder for this preprint (which was not certified by peer review) is the author/funder. All rights reserved. No reuse allowed without permission.

DHM relies on the interference between two waves: a coherent reference wave and a wave resulting from the light scattered by the object. The 3D reconstruction of objects featuring both weak and strong scattering compartments, e.g., tail and head of sperm, is challenging because interference patterns of strong scattering compartments conceal those patterns derived from weakly scattering objects. Additionally, DHM is very sensible to noise and 3D reconstruction from DHM data requires extensive computations.

A simple alternative to DHM is MFI. MFI produces a 3D image stack of the specimen by recording different focal planes simultaneously. An MFI device, placed into the light path between microscope and camera, splits the light collected by the objective and projects multiple focal images of the sample on distinct locations of the camera chip. However, this approach constrains the field-of-view (FOV) [13] and lowers the signal-to-noise ratio (SNR) when increasing the number of focal planes. Thus, state-of-art 3D tracking based on MFI requires bright fluorescent labels and is limited to either lower speeds, small sampled volumes, or low precision [13,15-19]. Here, we develop dark-field-microscopy-based MFI for label-free, long-term, and high-speed imaging at a high SNR and applicable over a large volume. Additionally, we introduce a 3D reconstruction method for MFI allowing to track spheres and to reconstruct filaments, such as flagella, at speeds of 500 Hz, with sub-micrometer precision, in a large FOV of up to 240 x 260 µm², and across a large depth of up to 21 µm.

Results

Assembling a broadly applicable MFI setup

We aim to establish an MFI system based on dark-field microscopy, as dark-field microscopy delivers high contrast images without any sample labeling. Generally, four alternative approaches to obtain information from different focal planes are applicable for imaging: (1) inserting an optical grating [13,18], (2) using a deformable mirror [20], (3) changing the optical

bioRxiv preprint doi: https://doi.org/10.1101/2020.05.16.099390; this version posted May 16, 2020. The copyright holder for this preprint (which was not certified by peer review) is the author/funder. All rights reserved. No reuse allowed without permission.

path length [14,16], and (4) by using lenses of different focal power [15,17,19]. Disadvantageously, optical gratings (approach (1)) are wavelength-dependent and have low optical efficiency. Deformable mirrors (approach (2)) are bulky, expensive, and highly wavelength-dependent, which prohibits their use for low-cost compact applications. Therefore, we here aim for an MFI system that is a combination of approaches (3) and (4) and thus, can be flexibly accommodated in different experimental set-ups. We use a multifocal adapter that splits the incoming light from the microscope into four light paths, which are projected to different quarters of the camera chip (Supplementary Fig. 1a). Four different focal planes of the specimen are obtained by inserting four lenses of different focal power into the individual light paths (Supplementary Fig. 1b and 1d). Restricting the number of focal planes to four minimizes the loss of SNR due to light splitting, while keeping the system low in complexity. Based on the thin-lens approximation, we can predict the defocusing of a pattern in the set-up based on the set of lenses and the magnification applied (Supplementary Fig. 1c and 1e). We assembled the multifocal adapter to study objects of millimeter to sub-micrometer size by changing the magnification (Supplementary Table 1). This flexibility enables studying fast-moving objects, ranging from whole animals to subcellular organelles.

Extended depth-of-field imaging of fast-moving objects

Long-term imaging of a fast-moving object with high spatial and temporal resolution is a common, but challenging requirement in microscopy. Imaging at high resolution with objectives of high magnification and numerical aperture, constrains the depth of field and the FOV. This increases the likelihood that the specimen exits the volume of observation during recording, limiting the duration of image acquisition. This limitation can be overcome by combining images acquired across the specimen using extended-depth-of-field (EDOF) algorithms [21]. However, this technique is not suited for fast-moving objects if different focal planes are acquired sequentially. MFI allows employing EDOF algorithms for fast-moving

bioRxiv preprint doi: https://doi.org/10.1101/2020.05.16.099390; this version posted May 16, 2020. The copyright holder for this preprint (which was not certified by peer review) is the author/funder. All rights reserved. No reuse allowed without permission.

objects (Fig. 1). We combine MFI (Fig. 1a) and EDOF (Fig. 1b) (see Materials and Methods) to study living specimens over a broad range of sizes: grooming *Drosophila melanogaster* (Supplementary Movie 1), foraging *Hydra vulgaris* (Supplementary Movie 2), crawling *Amoeba proteus* (Supplementary Movie 3), and beating human sperm (Supplementary Movie 4). In each of the four different focal planes, distinct structural features appear sharply (Fig. 1c). Using EDOF algorithms, these regions are assembled into one sharp image that reveals fine structural features, such as intracellular compartments (Supplementary Movie 3, Fig. 1b). The extended imaging depth allows tracking objects, even when the sample moves along the z-axis, with high speed, limited only by the applied camera, and over long time periods (Supplementary Movies 1-4).

High-precision 3D tracking with MFI

MFI has been applied for 3D tracking [13,15-19], but only at low resolution or small sampled volume, and relying on fluorescent labels. The image of an object, i.e. the sharpness, size, and intensity of the image, depends on the object's z-position relative to the focal plane. This correlation has been used to guess the third dimension from 2D microscopy images [22,23]. To determine the z-position, a precise calibration of the relationship between the image of the object and the z-position needs to be established. We combined this approach with MFI to achieve high-precision 3D tracking and illustrate the power of this concept by reconstructing the 3D movement of spherical objects (latex beads) and of filamentous structures (human sperm flagella) using label-free imaging by dark-field microscopy and the multifocal adapter.

To calibrate the relationship between the image and the z-position of a spherical object, we acquired multifocal z-stacks of non-moving 500-nm latex beads positioned across a depth of 21 µm; the step size, set by a piezo, was 0.1 µm. The bead image underwent two characteristic changes as the objective was moved: the radius of the bead image increased (Fig. 2a), and, as a result, the image intensity decreased (Fig. 2b). Both features are z-dependent and can be used

bioRxiv preprint doi: https://doi.org/10.1101/2020.05.16.099390; this version posted May 16, 2020. The copyright holder for this preprint (which was not certified by peer review) is the author/funder. All rights reserved. No reuse allowed without permission.

to determine the bead z-position. The z-position of a particle cannot be inferred unequivocally from a single plane, because, for any given bead radius, two possible z-positions exist (Fig. 2c). However, combining the information from multiple planes allows unequivocally localizing the particle in z (Fig. 2c). This appraoch also allows to combine multiple measurements of the z-position in different planes by, for example, applying Bayesian inference probability [24] or other statistical methods to improve the localization precision.

To determine the accuracy of inferring the beads z-position in our MFI setup based on the calibrated relationship between bead radius and z-position, we recorded a multifocal z-stack through immobilized latex beads using a piezo. Comparison of the inferred and piezo z-positions revealed a linear relationship (mean ± standard deviation of the slope: 0.98 ± 0.05, n = 7 beads from two different recordings). Based on linear fits with a slope of unity, we determined the z-localization error as 0.4 µm (Fig. 2d), which is below the Abbe resolution limit (2.1 µm; see Materials and Methods).

To prove the validity of our 3D-localization approach, we studied the stochastic Brownian motion of beads in suspension (Fig. 2e). The histograms of bead displacement across the three spatial dimensions (Fig. 2f) display a slight widening of the z-distribution due to localization errors. Yet, histograms are similar, indicating that stochastic bead motion was isotropic and normal distributed over all spatial coordinates. We conclude that MFI is highly suitable for 3D tracking.

High-precision 3D reconstruction of the flagella beat with MFI

Many eukaryotic cells, such as sperm or green algae, deploy flagella, lash-like appendages protruding from the cell surface. The 3D flagellar beat propels the cell on a 3D swimming path [23,25]. Because the beat frequency is high (up to 100 Hz) [6,7], the precise reconstruction of flagellar beating at high temporal and spatial resolution is challenging. The fastest calibrated 3D

bioRxiv preprint doi: https://doi.org/10.1101/2020.05.16.099390; this version posted May 16, 2020. The copyright holder for this preprint (which was not certified by peer review) is the author/funder. All rights reserved. No reuse allowed without permission.

reconstructions of human sperm achieved a temporal resolution of only 100 Hz. This temporal resolution allows to determine the beat frequency of human sperm, which is about 10 to 30 Hz [26], but it is insufficient to characterize the higher harmonics of the beat controlling sperm steering [6,27] or to track faster flagella, e.g. from *Anguilla* sperm (about 100 Hz) [7]. Recently, using Holography, flagella of human sperm have been reconstructed with a high temporal resolution (2,000 frames per second) albeit for a short time span of ca. 0.5 sec. Moreover, the tracking precision was not evaluated and the sampled volume was very small (ca. 30 x 45 x 16 µm³) [28] compared to the sperm's flagellum, which is about 50 µm long.

We aimed to establish MFI for reconstructing the 3D flagellar beat of human sperm at high speed, in a large FOV, and with high precision. To this end, we characterized the relationship between image and z-position of flagella. We acquired multifocal z-stacks of immotile sperm using the piezo-driven objective. Similar to the latex beads, the flagellum image displayed a characteristic widening (Fig. 3a) and a decrease of intensity (Fig. 3b) when imaged out of focus. We calibrated the functional dependency of these parameters along the flagellum for different z-positions, thus allowing for a precise 3D reconstruction of the flagellum (Fig. 3a, b).

We refined SpermQ, a software for analyzing motile cilia in 2D [29], to incorporate the analysis of multifocal images (SpermQ-MF); SpermQ-MF determines flagellar z-positions based on the calibrated relationship between flagellar width, position along the flagellum, and z-distance to the respective plane.

In each plane of multifocal images, SpermQ reconstructs the flagellum in 2D (x and y coordinates) with a localization precision below the resolution limit (Supplementary Fig. 2). To determine the accuracy of z-localization, we inferred the z-position of an immotile sperm using SpermQ-MF in multifocal z-stacks recorded with the piezo-driven objective (Fig. 3c). Inferred and piezo z-positions showed a linear relationship with a slope of unity (Fig. 3c). We estimated

bioRxiv preprint doi: https://doi.org/10.1101/2020.05.16.099390; this version posted May 16, 2020. The copyright holder for this preprint (which was not certified by peer review) is the author/funder. All rights reserved. No reuse allowed without permission.

an error of the z-localization of ~1 µm at the head and 0.6 µm at the principal piece; both resolutions are below the Abbe limit (2.1 µm; see Materials and Methods) (Fig. 3d).

3D reconstruction of the flagellar beat with MFI

Using the calibrated MFI setup and SpermQ-MF, we reconstructed the 3D flagellar beat of human sperm swimming in a 300 µm deep chamber at an acquisition rate of 500 volumes s^{-1} for about 2 s, i.e. the time it takes a sperm cell crossing the FOV of ca. 240 x 260 x 19 µm² (Fig. 4a, Supplementary Movie 5). Due to the precise localization of the flagellum, we can resolve the 3D flagellar beat in detail (Fig. 4b, c). The propagation of waves along the flagellum appeared as diagonal patterns in the kymograph of the z-position, highlighting the importance of including the z-position in the characterization of the flagellar beat (Fig. 4b). By visualizing the beat plane (Supplementary Movie 6), we show that sperm roll around their longitudinal axis. In conclusion, our MFI-based flagellar reconstruction allowed to characterize the flagellar beat of human sperm in a large sampled volume (240 x 260 x 19 µm³) that was ca. 55-times larger than the sampled volume shown in a recent DHM-based reconstruction of human sperm flagella (30 x 45 x 16 µm³)[28] and ca. 76-times larger than the sampled volume shown in a MFI-based reconstruction of fluorescently-labeled *Trypanosoma* and *Leishmania* flagella (ca. 80 x 35 x 5.6 µm³)[17]. Of note, this large volume is sampled at a high temporal resolution (500 Hz) and with a precision below the Abbe limit, while for the other reported setups the precision has not been determined [17,30].

3D reconstruction of fluid flow around a human sperm cell

The behaviour of ciliated cells and the underlying physics is of particular interest in cell biology and biotechnological applications. We are only beginning to understand how sperm manage to navigate through a highly complex environment like the female genital tract [31] or how motile cilia synchronize their beat to produce fluid flow[32]. A key to these phenomena has been attributed to the hydrodynamic interactions between motile cilia and between motile cilia and

bioRxiv preprint doi: https://doi.org/10.1101/2020.05.16.099390; this version posted May 16, 2020. The copyright holder for this preprint (which was not certified by peer review) is the author/funder. All rights reserved. No reuse allowed without permission.

their surroundings [4,32]. The fluid flow resulting from flagellar beating has been studied experimentally and theoretically. Experimental studies only resolved the 2D flow pattern for different microorganisms such as *Giardia lamblia* [33], *Chlamydomonas reinhardtii*, and *Volvox* [34]. The 2D flow profile around human sperm has been inferred from the flagellar beat [35], and the 3D profile from numeric simulations of the flagellar beat of sea urchin sperm near walls [36]. However, the predicted flow profiles have not been tested experimentally.

To visualize the 3D flow around human sperm with our MFI technique we used latex beads, whose relationship between radius and z-position had been previously calibrated (Fig. 5a, Supplementary Movie 7). To follow the direction of the bead movement relative to the sperm flagellum, we tethered the sperm head to the glass surface.

Bead tracking reveals long-range hydrodynamic interactions between sperm and beads (Fig. 5b). At large distances from the sperm cell, bead movement displayed a characteristic Brownian motion (Fig. 5c). Closer to the cell, beads displayed a random Brownian motion with a drift towards the sperm head (Fig. 5d) and away from the flagellar tip (Fig. 5e). Near the flagellum, beads described a fast 3D spiral-like movement resulting from the 3D flagellar beat (Fig. 5d-e).

In summary, we show that MFI, in combination with a calibration approach, allows a label-free characterization of fast biological processes, such as fluid flow or flagellar beating, with unprecedented spatial-temporal precision and in a large sampled volume.

Discussion

Here, we demonstrate a high-speed, label-free, 3D imaging technique sampling large volumes. By combining MFI with dark-field microscopy, we circumvent sample labeling while still obtaining a high signal-to-noise ratio. Our MFI system does not rely on any specialized equipment. To build our MFI system, we used a commercially available adapter that is

bioRxiv preprint doi: https://doi.org/10.1101/2020.05.16.099390; this version posted May 16, 2020. The copyright holder for this preprint (which was not certified by peer review) is the author/funder. All rights reserved. No reuse allowed without permission.

compatible with most microscopes and that allows to customize the focal distance between the different imaged planes by replacing the lenses inserted into the adapter. Similar adapters can also be easily designed and customized to the experimental needs with additive manufacturing (e.g. 3D printing). However, using a commercially available adapter allows to create a cost-effective 3D imaging device that does not require expertise in optics, making it affordable and accessible to a large scientific community. Furthermore, we demonstrate that the MFI system can be flexibly adapted to different size ranges from the nano- to millimeter-scale by changing the objective.

In MFI, the number of planes inversely correlates with the SNR and the size of the FOV as the light from the sample is shared across the different planes. Using four focal planes allows to sample a large FOV with a high SNR. However, state-of-the-art MFI systems employing four focal planes have been limited to a low depth of the sampled volume of below 6 µm, employed high-magnification objectives (≥ 60x) constraining the FOV (≤ 80 x 35 µm²), while achieving a speed of 200 frames per second [15,17]. We overcome these limitations with a new 3D reconstruction algorithm that allowed us to computationally achieve an unprecedented depth resolution below the Abbe limit while reaching a depth of the sampled volume of up to 21 µm, a FOV of up to 240 x 260 µm², and a speed of 500 frames per second. This represents a 3.5-fold increase of the depth of the sampled volume, a 22-fold increase of the FOV, and a 2.5-fold increase in sampling speed compared to the fastest reported MFI system [17].

We have demonstrated the applicability of our technique for a label-free 3D reconstruction of human sperm's flagellar beat with unprecedented tempo-spatial precision. Common methods to characterize 3D flagellar beating of mammalian sperm involved combinations of light microscopy with a piezo-driven objective or digital holographic microscopy (DHM), also known as holographic phase retrieval [30,37-41]. The piezo-driven method allows to acquire at 100 volumes s^{-1}, which represents a fifth of the sampling speed achieved by our method.

bioRxiv preprint doi: https://doi.org/10.1101/2020.05.16.099390; this version posted May 16, 2020. The copyright holder for this preprint (which was not certified by peer review) is the author/funder. All rights reserved. No reuse allowed without permission.

Additionally, acquisition of planes takes place at different time points, requiring high-speed high-sensitivity cameras recording 5,000 images s^{-1}, that are very expensive and thus, restrict the availability of this technique to only few labs [41]. DHM can provide the same temporal resolution as MFI; however, there are other factors that limit DHM. First, DHM is challenging when imaging strong- and weak-scattering objects at the same time, e.g. in contrast to MFI, DHM is not capable of reconstructing a "small" sperm cell close to a "large" egg cell. Second, DHM is not applicable to fluorescent objects, whereas, using different colors of labels, MFI could record multiple objects simultaneously. Third, DHM requires complex and extensive computational methods, while MFI does not. A state-of-the-art DHM-based reconstruction method for flagella featured a high temporal resolution (2,000 volumes s^{-1}) but a small sampled volume of ca. 30 x 45 x 16 μm^3 and the precision of the method was not reported[30]. Our technique for 3D reconstruction of human sperm provides a unique combination of a large sampled volume (ca. 240 x 260 x 19 μm^3), high precision below the Abbe limit (0.6 µm), and high speed (500 Hz), which outcompetes currently available alternative approaches.

Applying our technique to bead tracking allowed for the first time to record the fluid flow around a motile cilium, i.e. the human sperm flagellum, in 3D. Current techniques allowed to study the fluid flow surrounding flagellated microorganisms in 2D [33-35]. The 3D profile has only been estimated by numerical simulations of the 3D flagellar beat of sperm [36]. Here, we reveal 3D spiral-shaped flow patterns around sperm. Additionally, we show that fluid flow transports afar molecules to the flagellum. The flagellum acts as a propeller and a rudder, whose function is regulated by extracellular cues that act on intracellular signalling pathways [4]. Thus, it will be important to investigate in further studies how the spiral-shaped flow pattern and the transport of fluid to the flagellum impact the sensing of chemical or rheotactic cues by sperm for navigation to the egg. Combining MFI and fluorescence microscopy allows simultaneously recording the sperm flagellum and beads using different fluorescent labels. This will allow

bioRxiv preprint doi: https://doi.org/10.1101/2020.05.16.099390; this version posted May 16, 2020. The copyright holder for this preprint (which was not certified by peer review) is the author/funder. All rights reserved. No reuse allowed without permission.

revealing how a flow profile is generated by the 3D beat, and how fluid flow varies in time as the beat progresses [42].

By combining MFI with EDOF algorithms, we establish long-term visualization of low micro- to millimeter specimens, such as sperm or insects, respectively, at high recording speeds. We exemplify high-precision filament reconstruction and sphere tracking at the micrometer scale. The same concept is applicable at larger scales where 3D reconstruction methods for filamentous objects are similarly required. For instance, the presented MFI-based filament reconstruction method could be employed to study rodent whisking during active vibrissal sensing [43].

While we have concentrated here on label-free samples, our method has the potential to be adapted to fluorescently-labelled samples and to be combined with state-of-art computational techniques, such as deep learning. For instance, a deep-learning method for deducing z-positions from fluorescence microscopy images was recently described [44]. Our method could incorporate similar computational techniques to make use of the information provided by multiple planes for extending the z-range and enhancing the precision in fluorescence microscopy.

To conclude, our MFI approach opens new avenues to study fast biological processes at many different scales in 3D with high precision.

Material and Methods

Species

Amoeba proteus and *Hydra vulgaris* were purchased freshly before the experiments (Lebendkulturen Helbig, Prien am Chiemsee, Germany). *Drosophila melanogaster* were adults (> 2 days old). Human semen samples were donated by healthy adult males with their prior

bioRxiv preprint doi: https://doi.org/10.1101/2020.05.16.099390; this version posted May 16, 2020. The copyright holder for this preprint (which was not certified by peer review) is the author/funder. All rights reserved. No reuse allowed without permission.

written consent and the approval of the ethics committee of the University of Bonn (042/17). Sperm cells were purified by a "swim-up" procedure [45] using human tubular fluid (HTF) (in mM: 97.8 NaCl, 4.69 KCl, 0.2 $MgSO_4$, 0.37 KH_2PO_4, 2.04 $CaCl_2$, 0.33 Na-pyruvate, 21.4 lactic acid, 2.78 glucose, 21 HEPES, and 25 $NaHCO_3$ adjusted to pH 7.3–7.4 with NaOH).

Imaging

All images except those of *D. melanogaster* were acquired using an inverted microscope (IX71; Olympus, Japan) equipped with a dark-field condenser and a piezo (P-725.xDD PIFOC; Physik Instrumente, Germany) to adjust the axial position of the objective. For MFI, the multi-channel imaging device (QV-2, Photometrics, USA) was installed in front of a high-speed camera (PCO Dimax, Germany). Different objectives were used: 20x (UPLFLN, NA 0.5; Olympus, Japan), 10x (UPlanSapo, NA 0.4; Olympus, Japan), 4x (UPlanFLN, NA 0.13; Olympus, Japan). The total magnification could be increased with an additional 1.6x magnification lens. Human sperm, *Amoeba proteus*, and *Hydra vulgaris* were investigated in a custom-made observation chamber of 150 µm depth [29]. Images of *D. melanogaster* were recorded with a stereomicroscope (SZX12; Olympus, Japan), equipped with a DF PLAPO 1X PF lens (NA 0.11; Olympus, Japan).

Characteristics of the multifocal adapter

The multi-channel imaging device QV-2 (Photometrics, USA) was used to split the light coming from the microscope into four light paths (Supplementary Fig. 1a). The light within each optical path was projected to a different location on the camera chip. The focal length of each optical path was varied by an additional lens located at the position designed for holding filters in the QV-2. For measurements, a set of lenses with the following focal lengths was used (in mm): $f_1 = \infty$ (no lens), $f_2 = 1{,}000$, $f_3 = 750$, and $f_4 = 500$ (Supplementary Fig. 1a).

bioRxiv preprint doi: https://doi.org/10.1101/2020.05.16.099390; this version posted May 16, 2020. The copyright holder for this preprint (which was not certified by peer review) is the author/funder. All rights reserved. No reuse allowed without permission.

Calculation of the Abbe resolution limit

The Abbe limit was calculated as $r_z = \frac{n}{NA}\left[\frac{\lambda}{NA} + \frac{e_{\text{pixel}}}{M}\right]$, where λ is the wavelength, n is the refractive index, NA is the numerical aperture of the objective, e_{pixel} is the lateral pixel size, and M is the magnification of the objective.

Intensity normalization across planes

Local differences of image intensity in the four focal planes (Supplementary Fig. 3a) were measured by recording an image without a specimen and generating an intensity heat-map (Supplementary Fig. 3b). For normalization, pixel intensity was divided by the respective fractional intensity value in the heat-map (Supplementary Fig. 3c).

Alignment of plane images

The four focal planes were aligned at each time step using the ImageJ plugin *Multi-Stack Reg.* [46]. An alignment matrix was determined from the first time point and applied to all subsequent frames.

For the images of freely-swimming human sperm, an image of a calibration grid was recorded (Supplementary Fig. 4a) and processed in ImageJ by image segmentation (threshold algorithm *Li* [47], Supplementary Fig. 4b), skeletonization [48] (Supplementary Fig. 4c), and alignment (*Multi-Stack Reg* [46]; Supplementary Fig. 4d). The output alignment matrix was used for plane alignment.

Determination of the inter-plane distances

To determine the inter-plane distances, a series of multifocal images of a calibration grid at different positions set by a piezo was acquired. For each of the four planes it was determined the piezo position at which a reference grid was in focus. The focus position was defined as the position at which the grid image featured the highest standard deviation of pixel intensity [49].

bioRxiv preprint doi: https://doi.org/10.1101/2020.05.16.099390; this version posted May 16, 2020. The copyright holder for this preprint (which was not certified by peer review) is the author/funder. All rights reserved. No reuse allowed without permission.

From the differences in focus position between neighboring planes, the inter-plane distances were determined.

For low magnification (stereomicroscope, 4x), where the piezo range was insufficient for spanning all planes, the inter-plane distance was estimated manually by measuring the required focus displacement between two adjacent planes for sharp imaging of the specimen in each plane.

Simulating images produced by the multifocal adapter

Based on the inter-plane distances and the focal lengths of the lenses in the QV-2, we performed numerical calculations of images produced by the setup. The different imaging planes produced by the MFI setup were obtained with ray-optics calculations based on the thin-lens equation.

Defocusing was simulated by convolving the point-spread-function (PSF) with the sharpest image that we acquired of the calibration grid. We assumed a Gaussian PSF with transverse intensity distribution:

$$I_G(r,z) = \frac{w_0}{w(z)} e^{-\frac{r^2}{w(z)^2}}.$$

In the previous equation, $w(z) = w_0\sqrt{1+\left(\frac{z}{z_R}\right)^2}$ is the evolution of the Gaussian beam width with the propagation distance z, $z_R = \frac{\pi w_0^2}{\lambda}$ is the Rayleigh range, w_0 is the Gaussian beam width at the focal plane, and λ is the wavelength. w_0 is given by the optical resolution provided by the experimental set-up (Abbe limit, about 2.1 µm). Based on the resolution, the inter-plane distances, and the Rayleigh range z_R, we calculated the Gaussian beam width $w(z)$ and PSF at every z and for each plane.

bioRxiv preprint doi: https://doi.org/10.1101/2020.05.16.099390; this version posted May 16, 2020. The copyright holder for this preprint (which was not certified by peer review) is the author/funder. All rights reserved. No reuse allowed without permission.

Extended depth-of-field (EDOF)

Multifocal images were processed into extended depth-of-field (EDOF) images using the complex wavelet mode [21] of the ImageJ plugin "extended depth-of-field" by "Biomedical Imaging Group", EPFL, Lausanne. We created a customized version of this ImageJ plugin to enable automated processing of time series of image stacks.

Flow of latex beads in aqueous solution around a human sperm cell

Sperm were suspended in an HTF solution containing 100 µg/ml HSA (Ref. 9988, Irvine Scientific, USA) and 40 µg/ml carboxylate-modified latex beads of 0.5 µm diameter (C37481, Lot # 1841924, Thermo Fisher Scientific Inc., USA), and inserted into the custom-made observation chamber. Images were recorded with the 20x objective (NA 0.5) and the additional 1.6x magnification lens at 500 fps.

For each time-point, a maximum-intensity-projection across the four planes was generated. Next, to remove non-moving beads from the image, a time-average projection was subtracted from all time-points. To determine bead positions in x, y, and time, the thereby created subtracted maximum-intensity-projection time series was subjected to the FIJI plugin "TrackMate" [50] (settings: LoG detector, estimated blob diameter of 10 pixel, threshold of 50, sub-pixel localization).

Each bead's z-position was analyzed using a java-based custom-written ImageJ plugin using the "TrackMate"-derived xy and time coordinates as a template.

For each of the focal planes, all pixels within a radius of 10 px (about 3.4 µm) were subjected to an unconstraint 2D radial fit to retrieve the radius. The fit was developed as follows.

For a circle of radius R centered at $C = (C_0,C_1)$, the circle equation $(x-C_0)^2+(y-C_1)^2=R^2$ can be rewritten as $(2x)C_0+(2y)C_1+C_2=x^2+y^2$, where $C_2=R^2-C_0^2-C_1^2$. With the

bioRxiv preprint doi: https://doi.org/10.1101/2020.05.16.099390; this version posted May 16, 2020. The copyright holder for this preprint (which was not certified by peer review) is the author/funder. All rights reserved. No reuse allowed without permission.

coordinates of the pixel given, we can fit the transformed circle equation linearly to calculate the parameters C_0, C_1, and C_2. The linear fit is constructed into the matrix form $\mathbf{A}c = \mathbf{B}$, where $\mathbf{A} = \begin{pmatrix} x_1 & y_1 & 1 \\ \vdots & \vdots & \vdots \\ x_n & y_n & 1 \end{pmatrix}\mathbf{W}$, $\mathbf{B} = \begin{pmatrix} x_1^2 + y_1^2 \\ \vdots \\ x_n^2 + y_n^2 \end{pmatrix}\mathbf{W}$, and $\mathbf{W} = \begin{pmatrix} I^2(x_1, y_1) & & \\ & \ddots & \\ & & I^2(x_n, y_n) \end{pmatrix}$ is the weight matrix defined by the square of the pixel intensity. $c = \begin{pmatrix} C_0 \\ C_1 \\ C_2 \end{pmatrix}$ is the approximate solution of this over-determined equation, which can be calculated with least-squares principle. Finally, the circle radius R can be determined using the equation: $R = \sqrt{C_0{}^2 + C_1{}^2 + C_2}$.

If the quality of the fit $r^2 > 0.8$, the radius was used to infer the z-position. If, for a bead, the fit to the radial profile did not match the criterion in more than two planes, the bead was excluded from analysis and no z-position was determined. The z-position was determined for each remaining bead as follows. In each focal plane, a difference function of the determined bead radius and the plane's calibrated relationship between bead radius and z-position was determined. Each difference function shows two minima, which represent the two most probable z-positions (one located above and another below the focal plane). Finally, the position of the bead was unequivocally determined from the multiple measures of the z-positions across different planes: the combination of z-positions from the different planes with the lowest standard deviation was averaged into the final bead's z-position.

Images of immobilized beads at different heights set by a piezo-driven objective were used for calibration of z-positions. Radius profiles across z of seven different beads were aligned by minimizing the least-mean-square between all the planes. Finally, aligned profiles were averaged and smoothed.

bioRxiv preprint doi: https://doi.org/10.1101/2020.05.16.099390; this version posted May 16, 2020. The copyright holder for this preprint (which was not certified by peer review) is the author/funder. All rights reserved. No reuse allowed without permission.

Individual bead coordinates on each frame were connected to form tracks using custom-made software written in MATLAB. The software searched for the nearest particle across frames within a distance of less than 1.5 µm.

For characterizing Brownian motion, the normalized histogram of bead displacement along each dimension d ($d = x$, y, or z) of space was fitted to the characteristic probability density function of diffusive particles [51]:

$$P(d,t) = \frac{1}{\sqrt{4\pi Dt}} e^{-d^2/4Dt}$$

Reconstruction of the flagellar beat

To reconstruct the flagellar beat, we developed a fully-automated ImageJ plugin written in Java (SpermQ-MF). This plugin was based on SpermQ, a preexisting plugin for 2D analysis of flagellar beating [29]. The sharpest (highest standard deviation of pixel intensity) of the four plane images was subjected to the standard SpermQ workflow to reconstruct the flagellum in 2D. Next, the z-position of each point was determined using two methods based on the flagellar width or the pixel intensity.

For the method based on the width, a Gaussian curve was fitted to the image intensity in the direction normal to the flagellum at that particular point. The width of the resulting Gaussian was then converted into two z-positions (one located above and another below the focal plane) using the calibrated relationship between the flagellar width, the position on the flagellum, and the z-distance to the respective plane. Finally, the position of the flagellar point was unequivocally determined from the multiple measures of the z-positions across different planes.

For the z-localization method based on the changes of pixel intensity, we determined the intensity value of a given flagellar point in each plane by linear interpolation from the four surrounding pixels weighted by their distance to the given point. Next, each intensity value,

bioRxiv preprint doi: https://doi.org/10.1101/2020.05.16.099390; this version posted May 16, 2020. The copyright holder for this preprint (which was not certified by peer review) is the author/funder. All rights reserved. No reuse allowed without permission.

together with the focal position of the corresponding plane, formed a point in a coordinate system of focal position and intensity. A Gaussian curve was fitted to the resulting four points, whose center referred to the z-position. All determined z-positions were averaged and smoothed along the arc length as described [29]. Finally, z-positions were calibrated using recordings of non-motile sperm at different heights set by a piezo-driven objective. Calibrations from all different analyzed sperm (n = 12 sperm from five different donors) were averaged and smoothed by a 6x6 kernel median-filter.

Code and software availability

The developed ImageJ plugins along with the source code will be made accessible on GitHub upon publication.

Software

Image processing and analysis were performed in ImageJ (v1.52i, National Institutes of Health, Bethesda, MN, USA) and MATLAB 2018b (Mathworks). Calculations were performed in MATLAB 2018b (Mathworks), Rstudio (version 1.2.5019), and R (version 3.6.1). Plots and figures were generated using GraphPad Prism (Version 6.07, GraphPad Software, Inc., La Jolla, CA, USA), OriginPro (Version 9.0.0G, OriginLab Corporation, Northampton, USA), MATLAB 2018b (Mathworks), and Adobe Illustrator CS5 (Adobe Systems, Inc., v15.0.0, San Jose, CA, USA). The Java-based software was developed and compiled using Eclipse Mars.2 (Release 4.5.2, IDE for Java Developers, Eclipse Foundation, Inc., Ottawa, Ontario, Canada) and using parts of the source code of SpermQ (v0.1.7, [29]).

bioRxiv preprint doi: https://doi.org/10.1101/2020.05.16.099390; this version posted May 16, 2020. The copyright holder for this preprint (which was not certified by peer review) is the author/funder. All rights reserved. No reuse allowed without permission.

References

1 Eichorn, C. *et al.* How flies are flirting on the fly. *BMC Biol.* **15**, 2, doi:10.1186/s12915-016-0342-6 (2017).

2 Ellington, C. P. The novel aerodynamics of insect flight: applications to micro-air vehicles. *J. Exp. Biol.* **202**, 3439-3448 (1999).

3 Kojima, S., Yamamoto, K., Kawagishi, I. & Homma, M. The Polar Flagellar Motor of Vibrio cholerae Is Driven by an Na+ Motive Force. *J. Bacteriol.* **181**, 1927-1930 (1999).

4 Alvarez, L., Friedrich, B. M., Gompper, G. & Kaupp, U. B. The computational sperm cell. *Trends. Cell. Biol.* **24**, 198-207, doi:10.1016/j.tcb.2013.10.004 (2014).

5 Weisse, S. *et al.* A quantitative 3D motility analysis of Trypanosoma brucei by use of digital in-line holographic microscopy. *PloS one* **7**, e37296, doi:10.1371/journal.pone.0037296 (2012).

6 Saggiorato, G. *et al.* Human sperm steer with second harmonics of the flagellar beat. *Nature communication* **8**, 1415, doi:10.1038/s41467-017-01462-y (2017).

7 Gibbons, B. H., Baccetti, B. & Gibbons, I. R. Live and reactivated motility in the 9+0 flagellum of Anguilla sperm. *Cell. Motil.* **5**, 333-350, doi:10.1002/cm.970050406 (1985).

8 Shimmen, T. & Yokota, E. Cytoplasmic streaming in plants. *Curr. Opin. Cell. Biol.* **16**, 68-72, doi:10.1016/j.ceb.2003.11.009 (2004).

9 Su, T. W., Xue, L. & Ozcan, A. High-throughput lensfree 3D tracking of human sperms reveals rare statistics of helical trajectories. *Proc. Natl. Acad. Sci. U. S. A.* **109**, 16018-16022, doi:10.1073/pnas.1212506109 (2012).

10 Su, T. W. *et al.* Sperm trajectories form chiral ribbons. *Sci. Rep.* **3**, 1664, doi:10.1038/srep01664 (2013).

bioRxiv preprint doi: https://doi.org/10.1101/2020.05.16.099390; this version posted May 16, 2020. The copyright holder for this preprint (which was not certified by peer review) is the author/funder. All rights reserved. No reuse allowed without permission.

11 Wilson, L. G., Carter, L. M. & Reece, S. E. High-speed holographic microscopy of malaria parasites reveals ambidextrous flagellar waveforms. *Proc. Natl. Acad. Sci. U. S. A.* **110**, 18769-18774, doi:10.1073/pnas.1309934110 (2013).

12 Jikeli, J. F. *et al.* Sperm navigation along helical paths in 3D chemoattractant landscapes. *Nature communication* **6**, 7985, doi:10.1038/ncomms8985 (2015).

13 Abrahamsson, S. *et al.* Fast multicolor 3D imaging using aberration-corrected multifocus microscopy. *Nat. Methods* **10**, 60-63, doi:10.1038/nmeth.2277 (2013).

14 Jikeli, J. F., Pascal, R., Alvarez, L. & Honnef, R. Patent 102010049751 (2010).

15 Itano, M. S., Bleck, M., Johnson, D. S. & Simon, S. M. Readily Accessible Multiplane Microscopy: 3D Tracking the HIV-1 Genome in Living Cells. *Traffic* **17**, 179-186, doi:10.1111/tra.12347 (2016).

16 Prabhat, P., Ram, S., Ward, E. S. & Ober, R. J. Simultaneous imaging of different focal planes in fluorescence microscopy for the study of cellular dynamics in three dimensions. *IEEE Trans. Nanobioscience* **3**, 237-242, doi:10.1109/tnb.2004.837899 (2004).

17 Walker, B. J. & Wheeler, R. J. High-speed multifocal plane fluorescence microscopy for three-dimensional visualisation of beating flagella. *J. Cell. Sci.* **132**, doi:10.1242/jcs.231795 (2019).

18 Dalgarno, P. A. *et al.* Multiplane imaging and three dimensional nanoscale particle tracking in biological microscopy. *Opt. Express* **18**, 877-884, doi:10.1364/OE.18.000877 (2010).

19 Toprak, E., Balci, H., Blehm, B. H. & Selvin, P. R. Three-dimensional particle tracking via bifocal imaging. *Nano Lett.* **7**, 2043-2045, doi:10.1021/nl0709120 (2007).

bioRxiv preprint doi: https://doi.org/10.1101/2020.05.16.099390; this version posted May 16, 2020. The copyright holder for this preprint (which was not certified by peer review) is the author/funder. All rights reserved. No reuse allowed without permission.

20 Shain, W. J., Vickers, N. A., Goldberg, B. B., Bifano, T. & Mertz, J. Extended depth-of-field microscopy with a high-speed deformable mirror. *Opt. Lett.* **42**, 995-998, doi:10.1364/OL.42.000995 (2017).

21 Forster, B., Van De Ville, D., Berent, J., Sage, D. & Unser, M. Complex wavelets for extended depth-of-field: a new method for the fusion of multichannel microscopy images. *Microsc. Res. Tech.* **65**, 33-42, doi:10.1002/jemt.20092 (2004).

22 Rikmenspoel, R., van, H. & Eijkhout, P. Cinematographic observations of the movements of bull sperm cells. *Phys. Med. Biol.* **5**, 167-181, doi:10.1088/0031-9155/5/2/306 (1960).

23 Bukatin, A., Kukhtevich, I., Stoop, N., Dunkel, J. & Kantsler, V. Bimodal rheotactic behavior reflects flagellar beat asymmetry in human sperm cells. *Proc. Natl. Acad. Sci. U. S. A.* **112**, 15904-15909, doi:10.1073/pnas.1515159112 (2015).

24 MacKay, D. J. C. *Information theory, inference, and learning algorithms*. (Cambridge University Press, 2003).

25 Farthing, N. E. *et al.* Simultaneous two-color imaging in digital holographic microscopy. *Opt. Express* **25**, 28489-28500, doi:10.1364/OE.25.028489 (2017).

26 Gallagher, M. T., Cupples, G., Ooi, E. H., Kirkman-Brown, J. C. & Smith, D. J. Rapid sperm capture: high-throughput flagellar waveform analysis. *Hum. Reprod.* **34**, 1173-1185, doi:10.1093/humrep/dez056 (2019).

27 Gong, A. *et al.* The steering gaits of sperm. *Philos. Trans. R. Soc. Lond. B. Biol. Sci.* **375**, 20190149, doi:10.1098/rstb.2019.0149 (2020).

28 Dardikman-Yoffe, G., Mirsky, S. K., Barnea, I. & Shaked, N. T. High-resolution 4-D acquisition of freely swimming human sperm cells without staining. *Sci. Adv.* **6**, eaay7619, doi:10.1126/sciadv.aay7619 (2020).

bioRxiv preprint doi: https://doi.org/10.1101/2020.05.16.099390; this version posted May 16, 2020. The copyright holder for this preprint (which was not certified by peer review) is the author/funder. All rights reserved. No reuse allowed without permission.

29 Hansen, J., Rassmann, S., Jikeli, J. & Wachten, D. SpermQ–A Simple Analysis Software to Comprehensively Study Flagellar Beating and Sperm Steering. *Cells* **8**, 10 (2019).

30 Dardikman-Yoffe, G., Mirsky, S. K., Barnea, I. & Shaked, N. T. High-resolution 4D acquisition of freely swimming human sperm cells without staining. *arXiv* (2020).

31 Wachten, D., Jikeli, J. F. & Kaupp, U. B. Sperm Sensory Signaling. *Cold Spring Harb Perspect Biol* **9**, doi:10.1101/cshperspect.a028225 (2017).

32 Elgeti, J. & Gompper, G. Emergence of metachronal waves in cilia arrays. *Proc. Natl. Acad. Sci. U. S. A.* **110**, 4470-4475, doi:10.1073/pnas.1218869110 (2013).

33 Lenaghan, S. C., Davis, C. A., Henson, W. R., Zhang, Z. & Zhang, M. High-speed microscopic imaging of flagella motility and swimming in Giardia lamblia trophozoites. *Proc. Natl. Acad. Sci. U. S. A.* **108**, E550-558, doi:10.1073/pnas.1106904108 (2011).

34 Drescher, K., Goldstein, R. E., Michel, N., Polin, M. & Tuval, I. Direct measurement of the flow field around swimming microorganisms. *Phys. Rev. Lett.* **105**, 168101, doi:10.1103/PhysRevLett.105.168101 (2010).

35 Ishimoto, K., Gadelha, H., Gaffney, E. A., Smith, D. J. & Kirkman-Brown, J. Coarse-Graining the Fluid Flow around a Human Sperm. *Phys. Rev. Lett.* **118**, 124501, doi:10.1103/PhysRevLett.118.124501 (2017).

36 Elgeti, J., Kaupp, U. B. & Gompper, G. Hydrodynamics of sperm cells near surfaces. *Biophys. J.* **99**, 1018-1026, doi:10.1016/j.bpj.2010.05.015 (2010).

37 Gadêlha, H., Hernández-Herrera, P., Montoya, F., Darszon, A. & Corkidi, G. The human sperm beats anisotropically and asymmetrically in 3D. *bioRxiv*, 795245, doi:10.1101/795245 (2019).

bioRxiv preprint doi: https://doi.org/10.1101/2020.05.16.099390; this version posted May 16, 2020. The copyright holder for this preprint (which was not certified by peer review) is the author/funder. All rights reserved. No reuse allowed without permission.

38 Hernandez-Herrera, P., Montoya, F., Rendon-Mancha, J. M., Darszon, A. & Corkidi, G. 3-D Human Sperm Flagellum Tracing in Low SNR Fluorescence Images. *IEEE Trans. Med. Imaging* **37**, 2236-2247, doi:10.1109/TMI.2018.2840047 (2018).

39 Daloglu, M. U. *et al.* Label-free 3D computational imaging of spermatozoon locomotion, head spin and flagellum beating over a large volume. *Light Sci. Appl.* **7**, 17121, doi:10.1038/lsa.2017.121 (2018).

40 Muschol, M., Wenders, C. & Wennemuth, G. Four-dimensional analysis by high-speed holographic imaging reveals a chiral memory of sperm flagella. *PloS one* **13**, e0199678, doi:10.1371/journal.pone.0199678 (2018).

41 Silva-Villalobos, F., Pimentel, J. A., Darszon, A. & Corkidi, G. Imaging of the 3D dynamics of flagellar beating in human sperm. *Conference proceedings: Annual International Conference of the IEEE Engineering in Medicine and Biology Society. IEEE Engineering in Medicine and Biology Society* **2014**, 190-193, doi:10.1109/EMBC.2014.6943561 (2014).

42 Guasto, J. S., Johnson, K. A. & Gollub, J. P. Oscillatory flows induced by microorganisms swimming in two dimensions. *Phys. Rev. Lett.* **105**, 168102, doi:10.1103/PhysRevLett.105.168102 (2010).

43 Bush, N. E., Solla, S. A. & Hartmann, M. J. Whisking mechanics and active sensing. *Curr. Opin. Neurobiol.* **40**, 178-188, doi:10.1016/j.conb.2016.08.001 (2016).

44 Wu, Y. *et al.* Three-dimensional virtual refocusing of fluorescence microscopy images using deep learning. *Nat. Methods* **16**, 1323-1331, doi:10.1038/s41592-019-0622-5 (2019).

45 Strunker, T. *et al.* The CatSper channel mediates progesterone-induced Ca2+ influx in human sperm. *Nature* **471**, 382-386, doi:10.1038/nature09769 (2011).

bioRxiv preprint doi: https://doi.org/10.1101/2020.05.16.099390; this version posted May 16, 2020. The copyright holder for this preprint (which was not certified by peer review) is the author/funder. All rights reserved. No reuse allowed without permission.

46 Thevenaz, P., Ruttimann, U. E. & Unser, M. A pyramid approach to subpixel registration based on intensity. *IEEE Trans. Image Process* **7**, 27-41, doi:10.1109/83.650848 (1998).

47 Li, C. H. & Tam, P. K. S. An iterative algorithm for minimum cross entropy thresholding. *Pattern Recognit. Lett.* **19**, 771-776, doi:Doi 10.1016/S0167-8655(98)00057-9 (1998).

48 Arganda-Carreras, I., Fernández-González, R., Muñoz-Barrutia, A. & Ortiz-De-Solorzano, C. 3D reconstruction of histological sections: Application to mammary gland tissue. *Microsc. Res. Tech.* **73**, 1019-1029, doi:10.1002/jemt.20829 (2010).

49 Groen, F. C., Young, I. T. & Ligthart, G. A comparison of different focus functions for use in autofocus algorithms. *Cytometry* **6**, 81-91, doi:10.1002/cyto.990060202 (1985).

50 Tinevez, J. Y. *et al.* TrackMate: An open and extensible platform for single-particle tracking. *Methods* **115**, 80-90, doi:10.1016/j.ymeth.2016.09.016 (2017).

51 Berg, H. C. *Random Walks in Biology*. (1993).

Acknowledgement

This work was supported by the German Research Foundation (DFG) via the priority program SPP 1726 “Microswimmers” (L.A., U.B.K, J.F.J, D.W.), the Boehringer Ingelheim Fonds (J.N.H.), the Excellence Strategy – EXC2151 – 390873048 (D.W.), and the Alexander von Humboldt Foundation (A.T.).

Author Contribution

J.F.J, L.A., D.W., and U.B.K. conceived the project. J.N.H., J.F.J., L.A., and U.B.K. designed the experiments. J.N.H., J.F.J., A.G., and R.P. performed the experiments. J.N.H., L.A., J.F.J., and A.G. developed software to analyze the data. J.N.H., J.F.J., and L.A. analyzed the data.

bioRxiv preprint doi: https://doi.org/10.1101/2020.05.16.099390; this version posted May 16, 2020. The copyright holder for this preprint (which was not certified by peer review) is the author/funder. All rights reserved. No reuse allowed without permission.

A.T. performed theoretical estimations. J.N.H., L.A., J.F.J., and U.B.K. wrote the manuscript. All authors commented on and edited the text.

Competing Interests

The authors declare no competing financial interests.

bioRxiv preprint doi: https://doi.org/10.1101/2020.05.16.099390; this version posted May 16, 2020. The copyright holder for this preprint (which was not certified by peer review) is the author/funder. All rights reserved. No reuse allowed without permission.

Figures

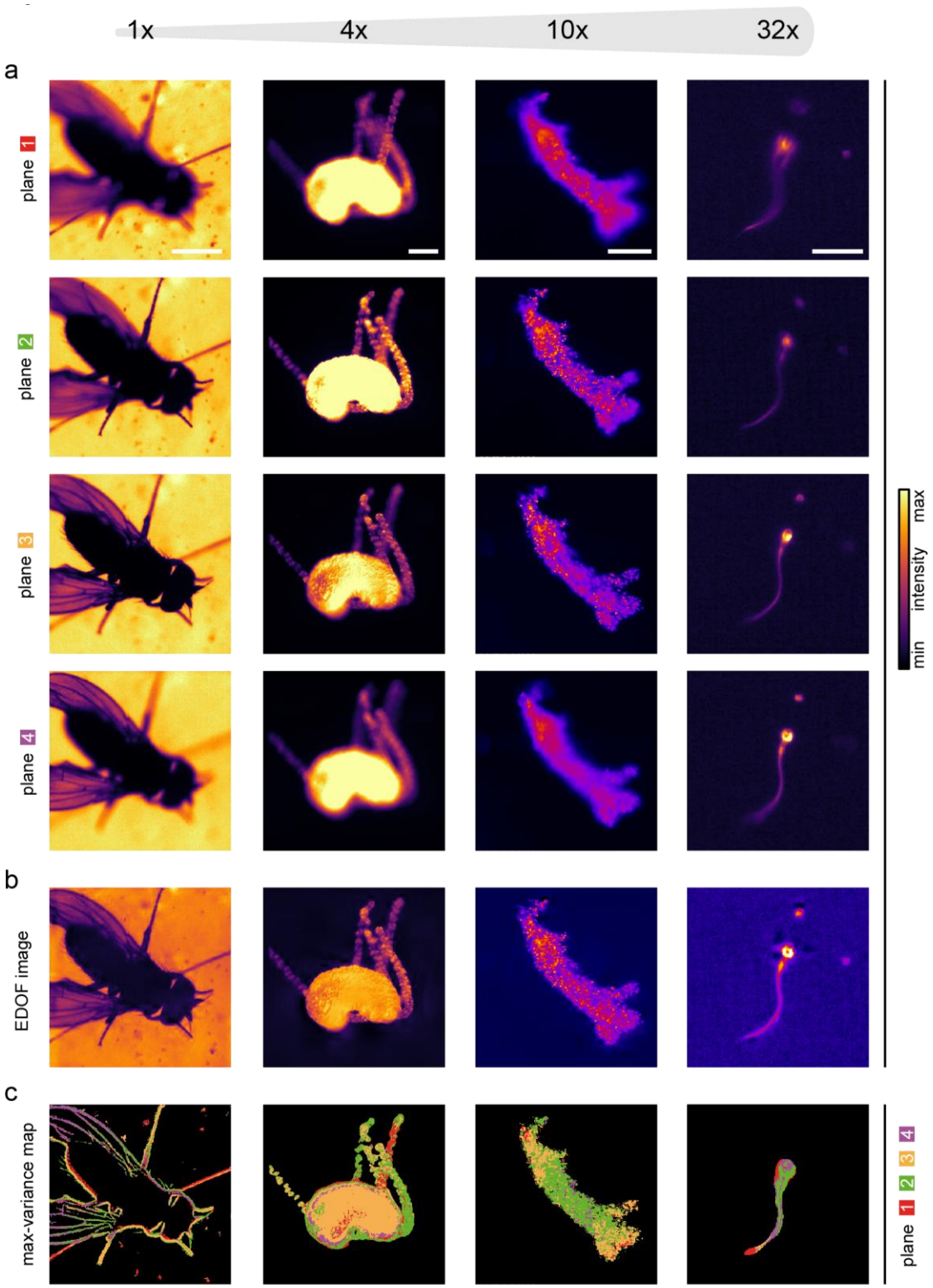

Figure 1 | Multifocal imaging enables high-speed, extended depth-of-field visualization.

(a) Multifocal images, acquired with the MFI system at various scales, demonstrate that MFI

bioRxiv preprint doi: https://doi.org/10.1101/2020.05.16.099390; this version posted May 16, 2020. The copyright holder for this preprint (which was not certified by peer review) is the author/funder. All rights reserved. No reuse allowed without permission.

can be used to simultaneously image fast-moving objects at different depths. Left to right: grooming *Drosophila melanogaster* (1x; scale bar 1 mm), foraging *Hydra vulgaris* (4x; scale bar 200 µm), crawling *Amoeba proteus* (10x; scale bar 100 µm), and swimming human sperm cell (32x; scale bar 20 µm). **(b)** Extended depth-of-field (EDOF) images produced from multifocal images shown in (a). **(c)** Max-variance maps showing for specific pixel positions the planes (color-coded) wherein the specimen appeared most sharp (sharpness determined as pixel variance), revealing a coarse feature localization of the object in z.

bioRxiv preprint doi: https://doi.org/10.1101/2020.05.16.099390; this version posted May 16, 2020. The copyright holder for this preprint (which was not certified by peer review) is the author/funder. All rights reserved. No reuse allowed without permission.

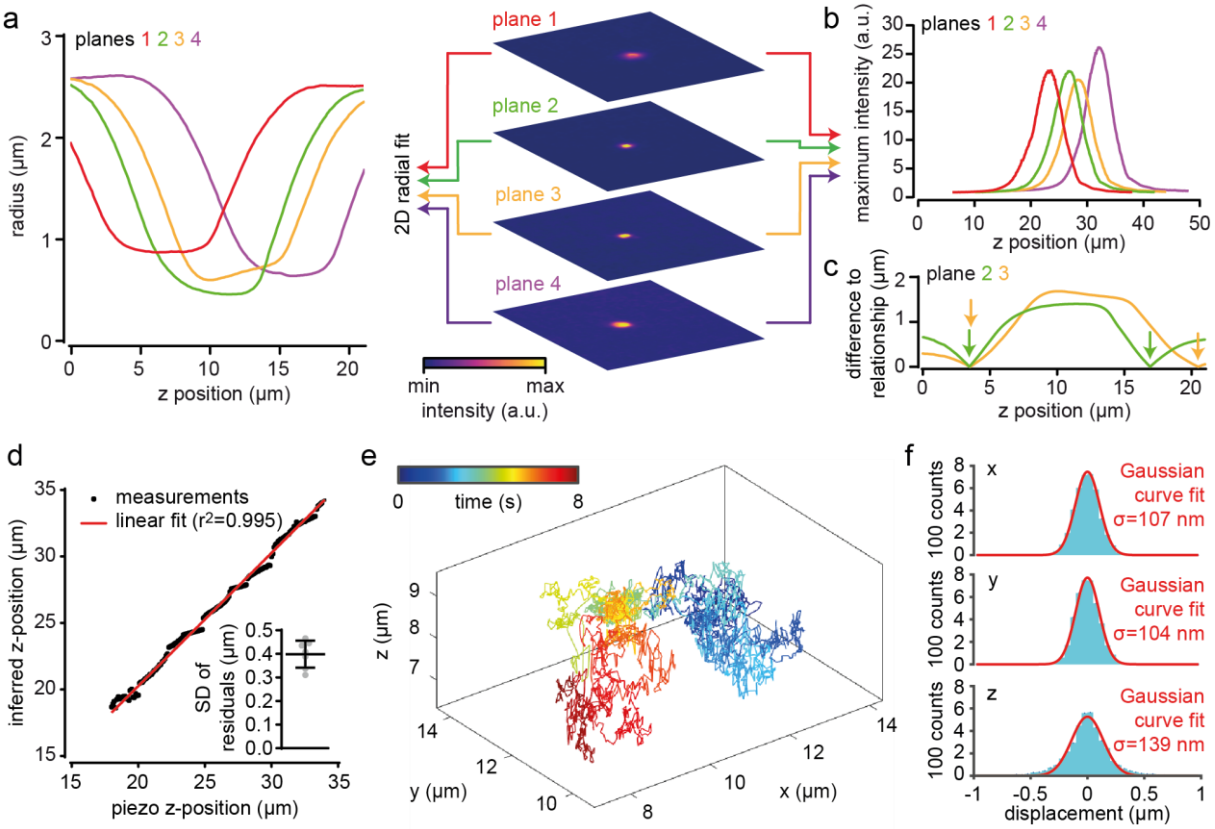

Figure 2 | Localizing latex beads in z using four focal planes.

(a-c) Characterizing the relationship between the image and the z-position of a latex bead (diameter 500 nm) in the MFI setup. **(a)** Bead radius determined by a 2D radial fit as a function of z-position; mean of seven beads (left). MF images of a latex bead at an exemplary z-position (right). **(b)** Maximum intensity of the bead image as a function of the bead's z-position in the four focal planes. **(c)** Difference between the measured bead radius and the calibrated relationship between bead radius and z-position (from panel (a)) reveals possible bead z-positions as minima (arrows). The overlay of the difference functions from two planes determines the bead's z-position unequivocally. **(d)** z-position of a non-moving bead inferred from MF images based on the calibrated relationship between bead radius and z-position during modulation of the objective z-position with a piezo (step size: 0.1 µm). A linear curve with a unity slope was fit to the data. Inset: Standard deviation (SD) of the residuals of linear curve fits with unity slope to the inferred z-positions during modulation of the objective z-position;

bioRxiv preprint doi: https://doi.org/10.1101/2020.05.16.099390; this version posted May 16, 2020. The copyright holder for this preprint (which was not certified by peer review) is the author/funder. All rights reserved. No reuse allowed without permission.

Mean ± standard deviation of n = 7 beads from two experiments. **(e)** Representative 3D trajectory of a freely diffusing latex bead, displaying a characteristic Brownian motion. The z-position of the bead was inferred by multifocal image analysis. **(f)** Characterization of the bead trajectory shown in (e), demonstrating that the displacement of the bead is normally distributed in x, y, and z.

bioRxiv preprint doi: https://doi.org/10.1101/2020.05.16.099390; this version posted May 16, 2020. The copyright holder for this preprint (which was not certified by peer review) is the author/funder. All rights reserved. No reuse allowed without permission.

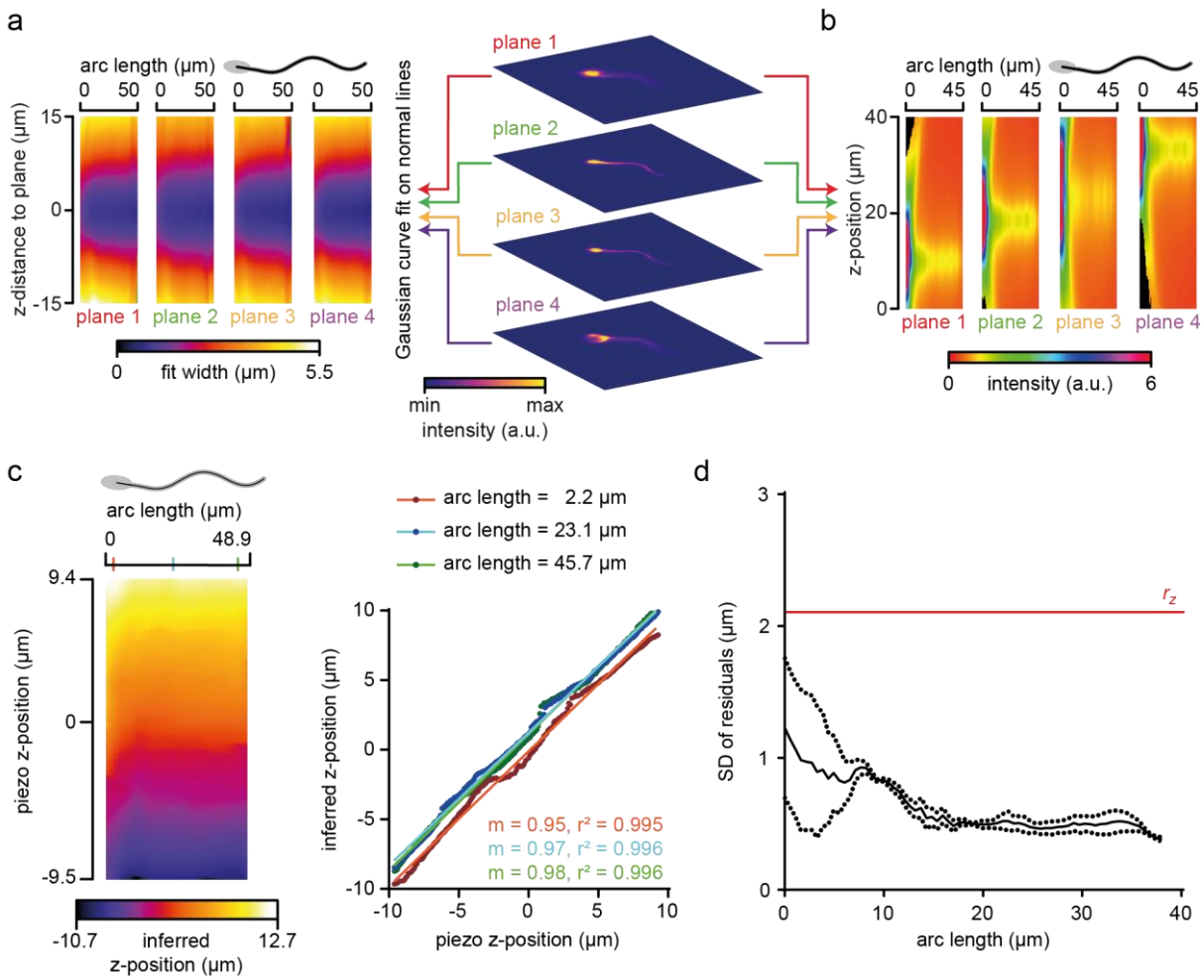

Figure 3 | Reconstructing flagellar z-positions using four focal planes.

(a-b) Characterizing the relationship between image and z-position of human sperm flagella in the MFI setup. **(a)** Flagellar width (color-coded), determined by a Gaussian curve fit on a normal to the flagellum, as a function of the flagellar position (arc length) and the z-distance to the respective plane (mean image of n = 12 sperm from five different donors). **(b)** Maximum intensity (color-coded) of the flagellum as a function of the flagellar position (arc length) and the z-position relative to the four planes. **(c)** z-position (color-coded) along the flagellum (arc length) of an immotile human sperm cell inferred from MF images based on the calibrated relationship between the flagellar width, position on the flagellum and z-distance to the respective plane during modulation of the objective z-position with a piezo (steps 0.1 µm; left). Colored ticks on the arc-length axis mark flagellar positions that are further analyzed by a linear

bioRxiv preprint doi: https://doi.org/10.1101/2020.05.16.099390; this version posted May 16, 2020. The copyright holder for this preprint (which was not certified by peer review) is the author/funder. All rights reserved. No reuse allowed without permission.

curve fit (right), revealing a linear relationship between the objective z-position and the z-position determined by MF image analysis (m: slope). **(d)** Standard deviation (SD) of the residuals of linear curve fits to data as exemplified in (c). Mean ± standard deviation of n = 3 sperm of different donors. Red line indicates the Abbe resolution limit in z (r_z) calculated for the respective objective.

bioRxiv preprint doi: https://doi.org/10.1101/2020.05.16.099390; this version posted May 16, 2020. The copyright holder for this preprint (which was not certified by peer review) is the author/funder. All rights reserved. No reuse allowed without permission.

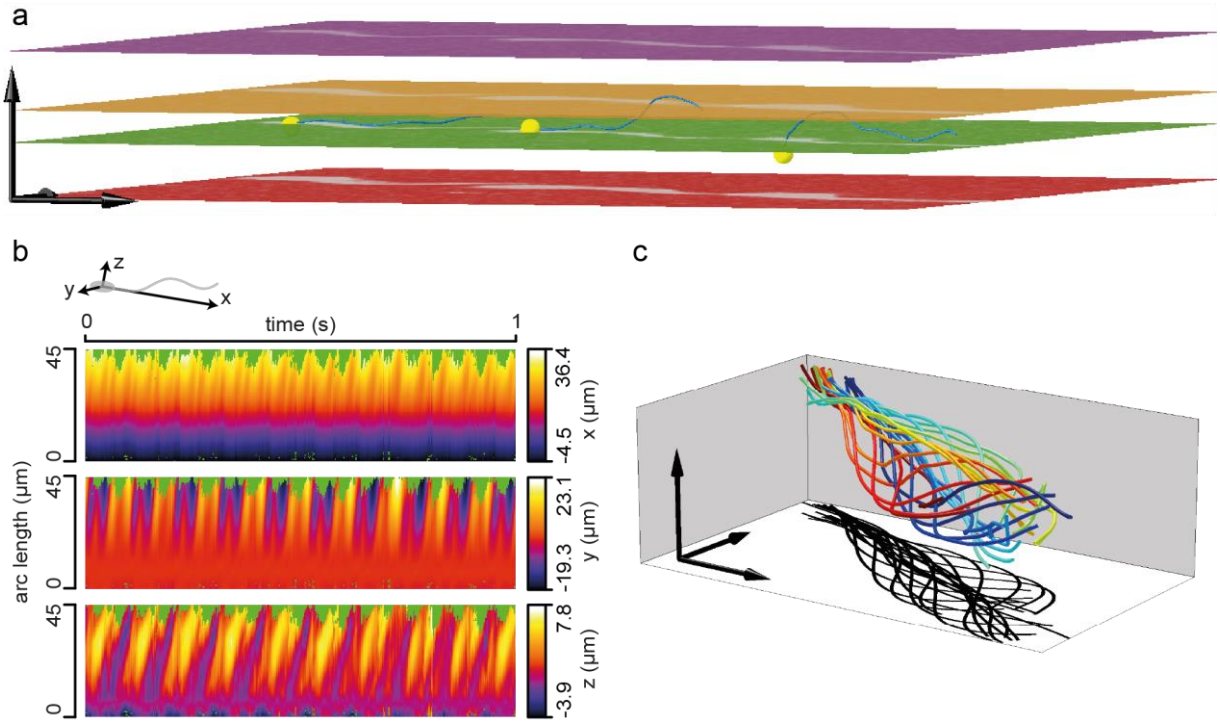

Figure 4 | 3D reconstruction of flagella from a swimming human sperm cell. (a) 3D visualization of the four planes (depicted in different colors) acquired by MFI and the flagellum reconstructed using SpermQ-MF and the calibrated relationship between flagellar width, position along the flagellum, and z-distance to the respective plane (Fig. 3a). Overlay of three exemplary time-points. Flagella indicated in blue. Positions of sperm heads indicated as yellow spheres. Arrows indicate 20 µm. **(b)** Kymographic representation of flagellar 3D coordinates (color-coded) in a reference system defined by the head-midpiece axis (see sketch on top). For better visualization, only the first second was plotted (reconstructed time span: 2.2 s). **(c)** 3D visualization of one beat cycle (time is color-coded). Arrows indicate 10 µm. Shadow indicates a projection of the flagellar beat to the xy-plane.

bioRxiv preprint doi: https://doi.org/10.1101/2020.05.16.099390; this version posted May 16, 2020. The copyright holder for this preprint (which was not certified by peer review) is the author/funder. All rights reserved. No reuse allowed without permission.

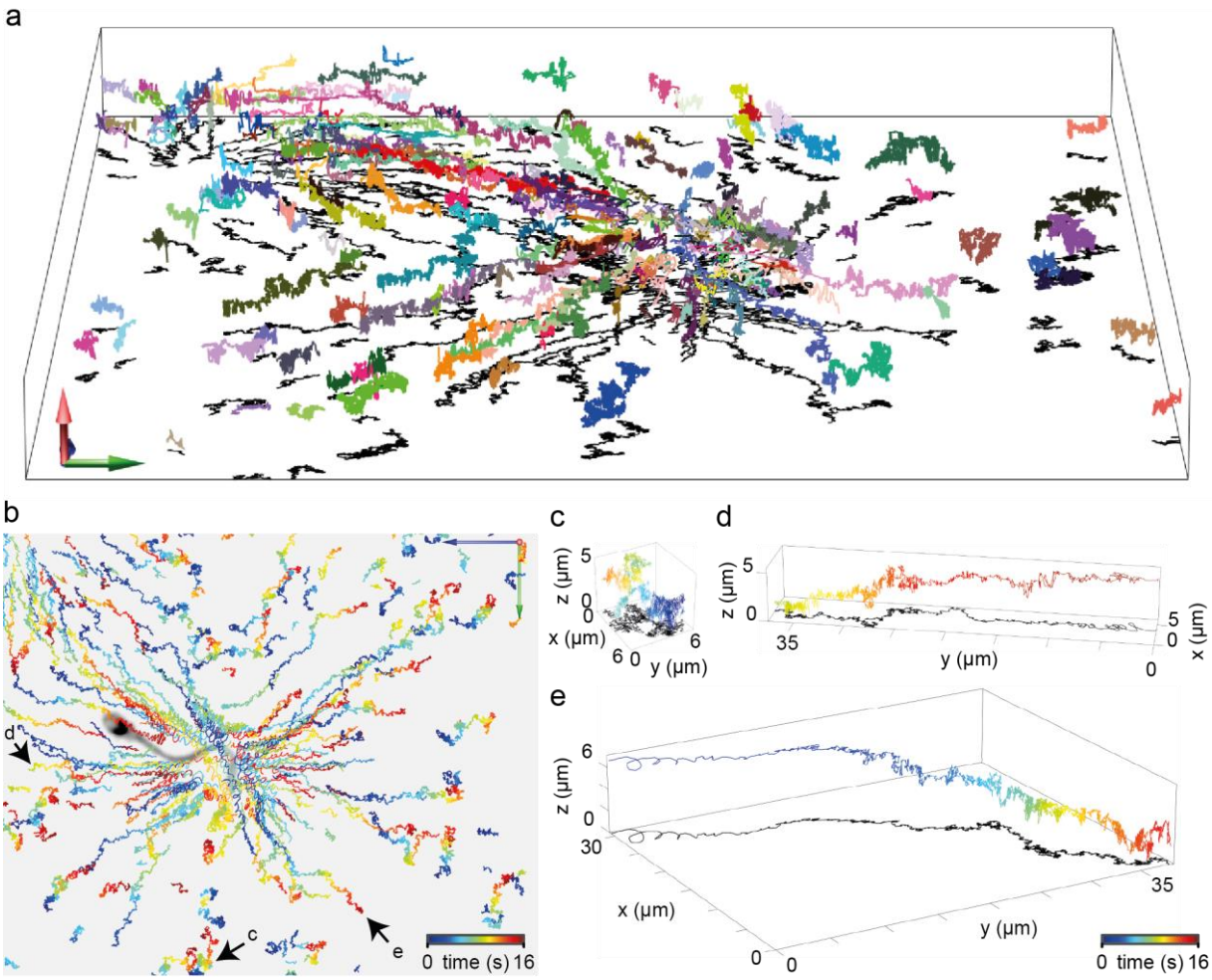

Figure 5 | 3D tracking of latex beads around a sperm cell. (a) Exemplary 3D trajectories of latex beads flowing around a human sperm cell tethered to the cover glass at the head. Trajectories were reconstructed from MF images using the ImageJ plugin "TrackMate" for xy-tracking and by inferring bead z-positions based on the calibrated relationship between bead radius and z-position (Fig. 2a). Each trajectory depicted in a different colour. Arrows indicate 10 µm. **(b)** Bead trajectories (color-coded by time) projected onto a plane image from the MF images showing the sperm cell (intensity inverted for better visualization). Black arrows mark trajectories shown in (c), (d), and (e). Coloured arrows indicate 20 µm. **(c)** Trajectory of a bead that is remote from the flagellum-driven fluid flow. **(d)** Trajectory of a bead that is attracted to the sperm cell. **(e)** Trajectory of a bead that is moving away from the flagellum. Close to the sperm flagellum (panel d: at times around 16 s; panel e: at times around 0 s), the beads displays

bioRxiv preprint doi: https://doi.org/10.1101/2020.05.16.099390; this version posted May 16, 2020. The copyright holder for this preprint (which was not certified by peer review) is the author/funder. All rights reserved. No reuse allowed without permission.

a 3D spiralling motion; far away from the sperm cell the beads show Brownian-like motion (panel c; panel d: at times around 16 s; panel e: at times around 0 s).